Atom probe tomography of interfaces in ceramic films and oxide scales

K. Stiller, M. Thuvander, I. Povstugar, P.P. Choi, and
H.-O. Andrén

Atomic-scale characterization of interfaces in ceramic materials is needed in order to fully understand their electronic, ionic, mechanical, magnetic, and optical properties. The latest development of laser-assisted atom probe tomography (APT), as well as new specimen preparation methods, have opened the realm of ceramics for structural and chemical characterization with high sensitivity and nearly atomic spatial resolution. This article reviews recent APT investigations of interfaces in thin nitride films and thermally grown oxides: TiAlN layers and oxide scales on alumina- and chromia-formers and Zr alloys. The selected examples highlight the role of interfaces in the decomposition of films and in transport processes.

Introduction

Engineering ceramics, such as oxides, nitrides, and carbides, represent an important material group used in electronic devices, aerospace components, cutting tools, and in various tribological applications. Crucial for the operation of energy-efficient power-generation technologies is to limit the thermal growth of oxides such as zirconia, alumina, and chromia. Atomic-scale characterization of interfaces in these materials is a prerequisite to fully understand their electronic, ionic, mechanical, magnetic, and optical properties.[1–3]

The only method that can be used to routinely analyze and map individual atoms in a material in three dimensions with nearly atomic resolution and with equal sensitivity for all elements is atom probe tomography (APT). For many years, this technique was mostly used for investigations of metallic materials because of the use of high-voltage pulses to evaporate ions from the specimen surface, which required the material to have high electrical conductivity ($>10^2$ S/cm).[4,5] Consequently, APT studies of insulating ceramics were not feasible except for investigations concerned with small oxide precipitates embedded in a metallic matrix,[6–9] or nanometer-thick oxide layers sandwiched between conducting layers.[4,10–12]

An alternative method to achieve field evaporation of ions using nanosecond laser pulses, proposed in the early 1980s,[13] could not be used for quantitative analysis in practice due to experimental difficulties with laser alignment and the operating parameters (pulsing energy, focus, pulsing rate, and laser wavelength). With the advent of faster laser systems (pico- and femtosecond), the focused ion beam milling technique for specimen preparation, and commercial APT instruments, the doors have been opened for three-dimensional analysis with nearly atomic resolution of insulating oxide and nitride ceramics, semiconductors, and even biological materials.[14–16]

During the last decade, several successful APT investigations of dielectric ceramics have been reported.[17–33] It is recognized, however, that quantitative studies of oxides and nitrides are challenging due to the complexity of the mass spectra (often containing peak overlaps), lower mass resolution and higher proportion of multiple events, and higher background level than for metallic materials, leading to a possible loss of information.[34,35]

Although it is now clear that field evaporation normally occurs due to heating generated by the laser pulse,[36] the mechanism by which materials transparent to light are able to absorb laser energy has been unclear. It appears that the application of a high DC voltage to a tip-shaped dielectric specimen induces a field within a screening distance of a few nm inside the dielectric that increases the light absorption up to values typical for metals. In addition, the bandgap in this zone is expected to decrease down to total band collapse.[37,38]

This explains the metallic-like behavior of wide bandgap materials in APT investigations. Moreover, the experimental parameters influencing the process of laser-assisted APT are not yet fully established. Recently, it has been shown that the optimal absorption of laser energy, beside intrinsic properties of the analyzed materials, is dependent not only on the wavelength of the laser pulse and its energy, but also on the tip radius and the shank angle of the needle-shaped APT specimen.[35,39–42]

This article reviews recent APT investigations of interfaces in thin nitride films and thermally grown oxides. As examples, studies of TiAlN layers and thermally grown oxide scales on alumina- and chromia-forming alloys and on Zr alloys are included. The selected examples highlight the role of interfaces in the decomposition of films and transport processes in the oxides.

Thermally grown alumina and chromia

Many alloys used for high-temperature applications form alumina (Al_2O_3) or chromia (Cr_2O_3) scales. These oxides are protective since they are dense, slow-growing, well bonded to the metal, and resistant to cracking and spallation. Diffusion along oxide grain boundaries (GBs) is recognized to be the rate-controlling transport mechanism that may be altered by the presence of alloying elements, but the exact mechanisms affecting diffusional fluxes still remain not entirely understood.
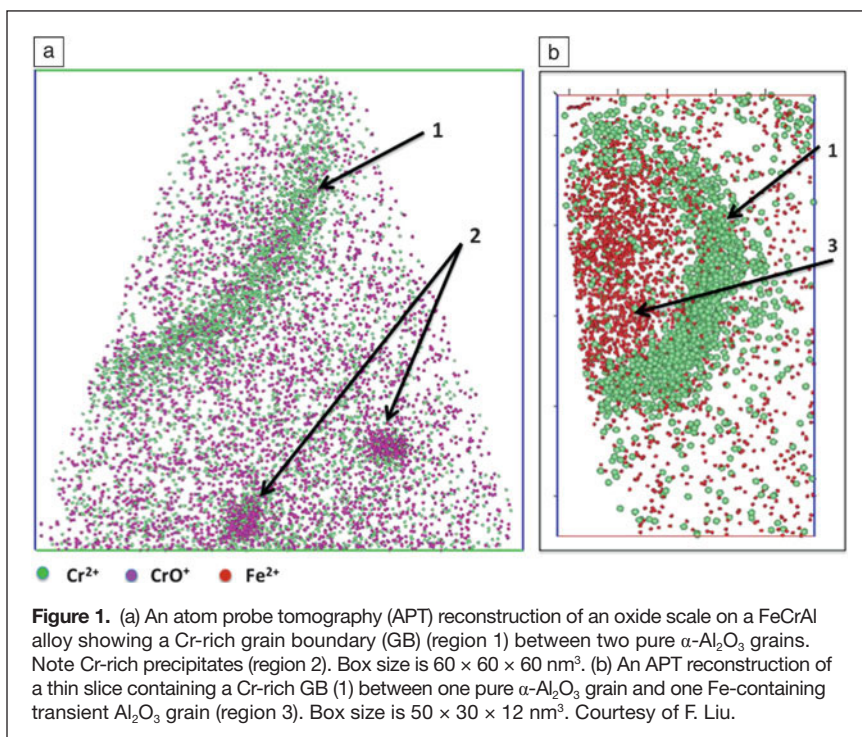
Exposure to air

One of the important issues concerning alumina is the fate of the base metal elements, most commonly Fe, Ni, or Cr, in the oxide. Recent APT studies[22,43] shed some light on this issue. For the first time, it was shown that Cr segregates (up to 12 at.% cationic [i.e., metal content in the oxide]) to oxide GBs during the initial stages of oxidation (1 h at 900°C) of FeCrAl, see **Figure 1**a. When the oxide scale is thin (approximately 100 nm), it consists of both transient (γ or θ) and stable (α) alumina grains. α−alumina grains are very pure, with less than 0.2 at.% (cationic) of Cr and Fe. At the same time, transient alumina grains may contain a substantial amount of Fe, ~8 at.% (cationic), Figure 1b. A possible explanation for this is that the transient alumina, known to be a cationic conductor, can dissolve high concentrations of divalent ions (i.e., Fe^{2+}) while trivalent ions (i.e., Cr^{3+}) are much less soluble. Thus, Cr segregates to the GBs or precipitates intragranularly as a result of the transformation of less stable Cr oxide created during rapid initial nonselective oxidation of the alloy. Indeed, nano-sized particles rich in Cr and some also rich in Fe were found in the middle part of the oxide scale, as seen in Figure 1a.

This picture is also supplemented by studies of 1.5-µm-thick α−alumina formed after prolonged oxidation (200 h at 1050°C in air) of a NiAl coating. Only a very pure Al_2O_3 (39 at.% Al, 61 at.% O) with practically no Cr (<0.1 at.%) is observed close to the oxide–metal interface. This is despite the presence of nano-sized Cr-rich precipitates in the metal close to this interface.[22] Due to low oxygen activity, the precipitates are not oxidized, but are only dissolved, when reached by the inward growing oxide. The excess Cr atoms do not segregate to the oxide GBs, but are incorporated into the precipitates inside the metal. Thus, it is believed that the influence of Cr segregation on oxide growth is important only in the very early stages of oxidation and that it weakens with the growth of the alumina scale.

The segregation of reactive elements (Zr, Y, Hf, Ce, etc.) from the alloy to the alumina GBs, often observed using analytical transmission electron microscopy (TEM), may also influence growth of the oxide.[44,45] However, a quantitative relationship between the segregation levels and oxide growth kinetics is still lacking. The first step in this direction was recently taken in an APT study that quantified segregation at several oxide GBs formed on a Ni-based coating.[24]

Carburization

Carburization of chromia is another problem, which is important for oxyfuel-fired (i.e., the fuel is burned in oxygen or an oxygen-enriched gas) energy production and solar thermal power generation, and which has been recently studied using APT.[32] The crucial issue in this case was to understand how carbon penetrates into a protective oxide scale. An APT investigation of an Fe–Cr model alloy exposed to Ar-20% CO_2 at

● Cr^{2+}　　● CrO^+　　● Fe^{2+}

Figure 1. (a) An atom probe tomography (APT) reconstruction of an oxide scale on a FeCrAl alloy showing a Cr-rich grain boundary (GB) (region 1) between two pure α-Al_2O_3 grains. Note Cr-rich precipitates (region 2). Box size is 60 × 60 × 60 nm³. (b) An APT reconstruction of a thin slice containing a Cr-rich GB (1) between one pure α-Al_2O_3 grain and one Fe-containing transient Al_2O_3 grain (region 3). Box size is 50 × 30 × 12 nm³. Courtesy of F. Liu.

650°C revealed the occurrence of 1.6×10^{20} atoms cm^{-3} carbon at oxide GBs. This is three orders of magnitude greater concentration than that of intragranular carbon, revealing that oxide GBs are pathways for the diffusion of this species.

Zirconia formed by water corrosion

Zirconium alloys used for cladding tubes for fuel rods in light water nuclear reactors form an oxide scale upon oxidation in water at high pressures and temperatures. The oxide mostly consists of monoclinic zirconia with a columnar grain structure, and the small oxide grain width (20–30 nm) makes GB transport a possible pathway for both oxygen and hydrogen ingress. APT analysis of an oxide formed in a steam autoclave at 400°C and 10.3 MPa showed that OH$^+$ ions were detected at planar features, assumed to be oxide GBs, parallel to the specimen axis.[29] To exclude the possibility that these ions are created by adsorption of the low partial pressure of hydrogen gas present in the APT vacuum chamber, an oxide formed in a heavy water autoclave was also analyzed. In this oxide, planar features contained deuterium, demonstrating that hydrogen from the water actually is transported along (hydroxylated) oxide GBs, **Figure 2**a–b.

APT of the underlying metal showed that the minor alloying elements Fe and Ni segregated to sub-GBs in the metal and that the inward-growing oxide inherits these GBs,[30] Figure 2c. Atomistic calculations have shown that Fe in an oxide GB acts as a reduction site for hydrogen, forming hydrogen gas and preventing hydrogen absorption in the metal, whereas Ni has the opposite effect, promoting hydrogen absorption.[46]

This explains the known effect of Ni addition to increase hydrogen pickup during corrosion in water of zirconium alloys. The distribution of tin (Sn) was also studied with APT.[31] Sn completely dissolves in the metal, and as the oxide front advances, Sn first dissolves in the zirconia, but gradually forms metallic clusters and precipitates. In particular, small clusters of Sn form at oxide GBs, but the clusters oxidize further away from the metal–oxide interface where the oxygen potential is higher.[31]

Interface-directed spinodal decomposition in TiAlN/CrN multilayer hard coatings

Nanometer-scale nitride multilayers such as TiAlN/CrN are excellent candidate materials as hard coatings for cutting tools due to their outstanding combination of hardness and oxidation resistance. However, they exhibit only limited thermal stability and start to degrade at 700–800°C despite their high melting point. In one study, Ti$_{0.75}$Al$_{0.25}$N/CrN multilayer coatings with B1 (fcc-like) structure, a bilayer period of 9 nm and a total thickness of 2 μm were sputter-deposited on a steel substrate and investigated at temperatures of 600–1000°C using APT to understand the mechanisms responsible for their thermal degradation.[27]

An APT elemental map for the as-deposited coating is presented in **Figure 3**a showing alternating CrN and TiAlN layers. The elemental distribution within the TiAlN layers is nearly homogenous despite a miscibility gap across the entire Ti:Al compositional range. Below 700°C, no compositional changes occurred in the studied multilayers. After annealing at 700°C for 1 h, each TiAlN layer turned into a triple-layer structure consisting of a Ti-rich layer confined by two Al-rich layers. The corresponding Al concentration profiles were asymmetric and showed local minima close to the center of the original TiAlN layers (Figure 3b). This stage of decomposition proceeded continuously and uniformly across the coating depth, with no indication of in-plane compositional fluctuations. Such decomposition behavior with smooth compositional gradients is characteristic of a spinodal mechanism rather than discontinuous nucleation and growth.[28,47]

The observed compositional fluctuations are, however, not typical of an isotropic spinodal mechanism, as there is a clear preferential direction for uphill diffusion perpendicular to the layers. Instead, they resemble surface-directed spinodal decomposition, which was discovered earlier in metallic or ceramic materials.[48,49] This mechanism is linked to the bias of the free energy of the system due to a contribution from the surface energy term. Similarly, interfacial energy can provide the observed preferential direction for uphill
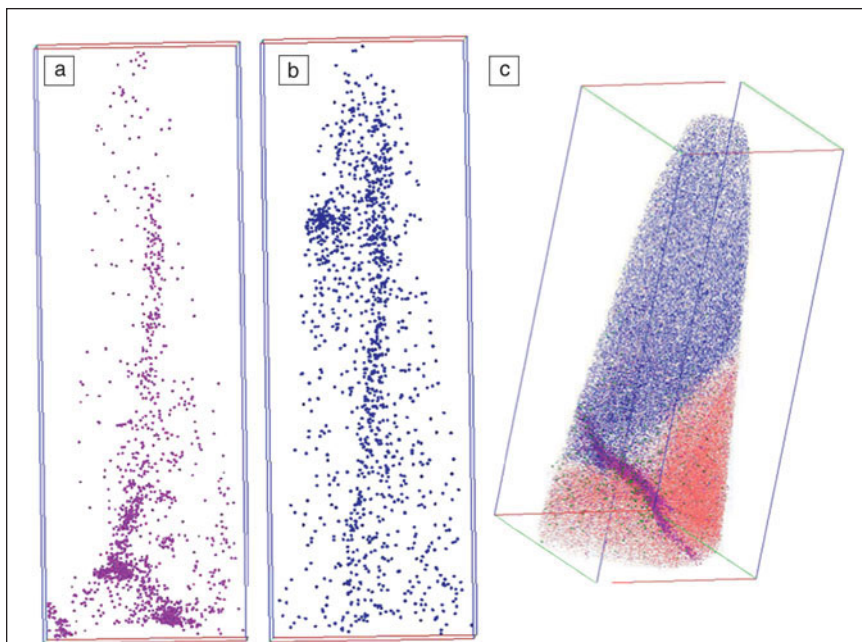

Figure 2. Atom probe tomography reconstruction of grain boundaries (GBs) in zirconia, showing enrichment of (a) Fe and (b) deuterium (OD$^+$) along the same boundary in the oxide; (c) shows segregation of Fe (purple) and Ni (green) to a sub-GB in the metal (red) that is inherited by the GB in the oxide (blue). Box sizes in (a) and (b) are 65 × 65 × 195 nm^3; in (c) 140 × 140 × 330 nm^3. Courtesy of G. Sundell.
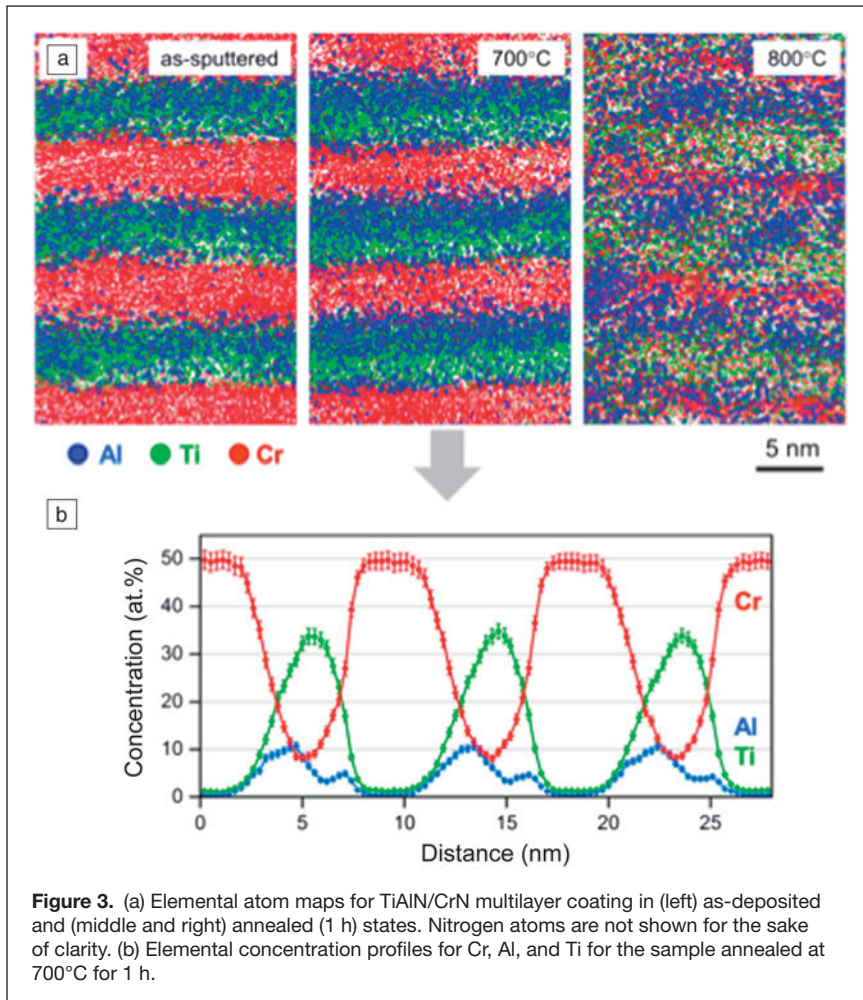
Figure 3. (a) Elemental atom maps for TiAlN/CrN multilayer coating in (left) as-deposited and (middle and right) annealed (1 h) states. Nitrogen atoms are not shown for the sake of clarity. (b) Elemental concentration profiles for Cr, Al, and Ti for the sample annealed at 700°C for 1 h.

Conclusions

The examples featured in this article demonstrate that invaluable information on atomic-scale microstructure of ceramics can be obtained using laser-assisted APT. In oxide scales, the transport properties are influenced by the local chemistry at the GBs. In nitride multilayer thin films, the properties are affected by spinodal decomposition, increasing the number of interfaces on a nanometer scale. The greatest challenge for future APT advancement is the low thermal conductivity of many ceramics, which at present severely restricts APT quantification capabilities. This could be improved by developing more sophisticated data analysis methods or by increasing the thermal conductivity of APT specimens, for example, by metal-coating the specimen shank.
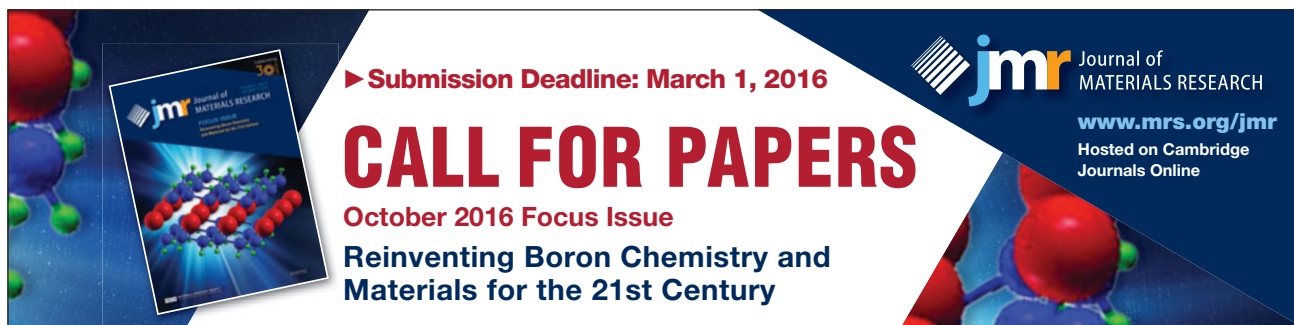
Acknowledgments

References

1. "Coated Carbide, Cermet, and Ceramic Tool Materials," in *ASM Specialty Handbook: Tool Materials*, J.R. Davies, Ed., (ASM International, Materials Park, OH, 1995), pp. 77–84.
2. C. Lemaignan, A.T. Motta, "Zirconium Alloys in Nuclear Applications," in *Materials Science and Technology, A Comprehensive Treatment*, R.W. Cahn, P. Haasen, E.J. Kramer, Eds. (VCH, Weinheim, Germany, 1994), vol. 10B.
3. M. Schütze, W.J. Quadakkers, Eds., *Novel Approaches to Improving High-Temperature Corrosion Resistance* (Woodhead Publishing, Cambridge, England, 2008).
4. C. Oberdorfer, P. Stender, C. Reinke, G. Schmitz, *Microsc. Microanal.* **13**, 342 (2007).
5. A.J. Melmed, M. Martinka, S.M. Girvin, T. Sakurai, Y. Kuk, *Appl. Phys. Lett.* **39**, 16 (1981).
6. J.T. Sebastian, A. Assaban, D.N. Seidman, B.J. Kooi, J.T.M. de Hosson, *Interface Sci.* **9**, 199 (2001).
7. J.T. Sebastian, J. Rusing, O.C. Hellman, D.N. Seidman, W. Vriesendrop, B.J. Kooi, J.T.M. de Hosson, *Ultramicroscopy* **89**, 203 (2001).
8. C. Kluthe, T. Al-Kassab, R. Kirchheim, *Mater. Sci. Eng. A* **353**, 112 (2003).
9. E.A. Marquis, *Appl. Phys. Lett.* **93**, 181904 (2008).
10. B. Mazumder, A. Vella, B. Deconihout, T. Al-Kassab, *Ultramicroscopy* **111**, 571 (2011).
11. T.F. Kelly, D.J. Larson, K. Thompson, R.L. Alvis, J.H. Bunton, J.D. Olson, B.P. Gorman, *Annu. Rev. Mater. Res.* **37**, 681 (2007).
12. M. Kuduz, G. Schmitz, R. Kirchheim, *Ultramicroscopy* **101**, 197 (2004).
13. G.L. Kellog, T.T. Tsong, *J. Appl. Phys.* **51**, 1184 (1980).
14. L.M. Gordon, D. Joester, *Nature* **469**, 194 (2011).
15. L.M. Gordon, L. Tran, D. Joester, *ACS Nano* **6**, 10667 (2012).
16. J. Karlsson, G. Sundell, M. Thuvander, M. Andersson, *Nano Lett.* **14**, 4220 (2014).
17. D.J. Larson, R.L. Alvis, D.F. Lawrence, T.J. Prosa, R.M. Ulfig, D.A. Reinhard, P.H. Clifton, S.S.A. Gerstl, J.H. Bunton, D.R. Lenz, T.F. Kelly, K. Stiller, *Microsc. Microanal.* **14**, 1254 (2008).
18. A. Vella, B. Mazumder, G. Da Costa, B. Deconihout, *J. Appl. Phys.* **110**, 044321 (2011).
19. K. Hono, T. Ohkubo, Y.M. Chen, M. Kodzuka, K. Oh-ishi, H. Sepehri-Amin, F. Li, T. Kinno, S. Tomiya, Y. Kanitani, *Ultramicroscopy* **111**, 576 (2011).
20. E.A. Marquis, N.A. Yahya, D.J. Larson, M.K. Miller, R.I. Todd, *Mater. Today* **13**, 34 (2010).

Al diffusion in order to minimize the total free energy (e.g., by minimizing the local residual stresses [usually large in sputter-deposited films]) at interfaces due to Al and Ti(Cr) atom size mismatch. Here, the mechanism should be referred to as interface-directed spinodal decomposition, since decomposition proceeds in the presence of interfaces instead of a free surface. The asymmetry of the decomposed TiAlN layers originates from inhomogeneous Al distribution in the as-sputtered state, which can, in turn, arise due to surface-directed Al diffusion under sputter deposition on a relatively hot substrate (300°C). It should be noted that at this stage, x-ray diffraction measurements and TEM observations showed almost no changes compared to the as-sputtered coating, revealing the usefulness of APT for the characterization of spinodal decomposition phenomena.

An increase in annealing time or temperature resulted in a transition from interface-directed to a common isotropic mechanism for TiAlN/CrN multilayers. Numerous areas with increased Al concentration were observed after annealing at 800°C for 1 h (see Figure 3a), typical of spinodal decomposition in bulk TiAlN.[28]

21. Y.M. Chen, R.C. Reed, E.A. Marquis, *Scr. Mater.* **67**, 779 (2012).
22. K. Stiller, L. Viskari, G. Sundell, F. Liu, M. Thuvander, H.-O. Andrén, D.J. Larson, T. Prosa, D. Reinhard, *Oxid. Met.* **79**, 227 (2013).
23. Y. Dong, A.T. Motta, E.A. Marquis, *J. Nucl. Mater.* **442**, 270 (2013).
24. Y.M. Chen, R.C. Reed, E.A. Marquis, *Oxid. Met.* **82**, 457 (2014).
25. L. Viskari, M. Hornqvist, K. Moore, Y. Cao, K. Stiller, *Acta Mater.* **61**, 3630 (2013).
26. S. Lozano-Perez, T. Yamada, T. Terachi, M. Schroder, C.A. English, G.D.W. Smith, C.R.M. Grovenor, B.L. Eyre, *Acta Mater.* **57**, 5361 (2009).
27. I. Povstugar, P.P. Choi, D. Tytko, J.P. Ahn, D. Raabe, *Acta Mater.* **61**, 7534 (2013).
28. L.J.S. Johnson, M. Thuvander, K. Stiller, M. Oden, L. Hultman, *Thin Solid Films* **520**, 4362 (2012).
29. G. Sundell, M. Thuvander, A.K. Yatim, H. Nordin, H.-O. Andrén, *Corros. Sci.* **90**, 1 (2015).
30. G. Sundell, M. Thuvander, H.-O. Andrén, *Corros. Sci.* **65**, 10 (2012).
31. G. Sundell, M. Thuvander, H.-O. Andrén, *J. Nucl. Mater.* **456**, 409 (2015).
32. D.J. Young, T.D. Nguyen, P. Felfer, J. Zhang, J.M. Cairney, *Scr. Mater.* **77**, 29 (2014).
33. J.-H. Kim, B.K. Kim, D.-I. Kim, P.P. Choi. D. Raabe, K.-W. Yi, *Corros. Sci.* **96**, 52 (2015).
34. T. Kinno, M. Tomita, T. Ohkubo, S. Takeno, K. Hono, *Appl. Surf. Sci.* **290**, 194 (2014).
35. A. Devaraj, R. Colby, W.P. Hess, D.E. Perea, S. Thevuthasan, *J. Phys. Chem. Lett.* **4**, 993 (2013).
36. F. Vurpillot, J. Houard, A. Vella, B. Deconihout, *J. Phys. D Appl. Phys.* **42**, 125502 (2009).
37. E.P. Silaeva, L. Arnoldi, M.L. Karahka, B. Deconihout, A. Menand, H.J. Kreuzer, A. Vella, *Nano Lett.* **14**, 6066 (2014).
38. G. Greiwe, Z. Balogh, G. Schmitz, *Ultramicroscopy* **141**, 51 (2014).
39. L. Arnoldi, A. Vella, J. Houard, B. Deconihout, *Appl. Phys. Lett.* **101**, 153101 (2012).
40. J.H. Bunton, J.D. Olson, D.R. Lenz, T.F. Kelly, *Microsc. Microanal.* **13**, 418 (2007).
41. Y. Amouyal, D.N. Seidman, *Microsc. Microanal.* **18**, 971 (2012).
42. M.D. Mulholland, D.N. Seidman, *Microsc. Microanal.* **17**, 950 (2011).
43. F. Liu, M. Halvarsson, K. Hellström, J.E. Svensson, L.G. Johansson, *Oxid. Met.* **83**, 441 (2015).
44. J.A. Haynes, B.A. Pint, K.L. More, Y. Zhang, I.G. Wright, *Oxid. Met.* **58**, 513 (2002).
45. K.A. Unocic, B.P. Pint, *Surf. Coat. Technol.* **237**, 8 (2013).
46. M. Lindgren, I. Panas, *RSC Adv.* **3**, 21613 (2013).
47. Q. Chen, B. Sundman, *J. Phase Equilib.* **19**, 146 (1998).
48. K.T. Moore, W.C. Johnson, J.M. Howe, H.I. Aaronson, D.R. Veblen, *Acta Mater.* **50**, 943 (2002).
49. J. Liu, X. Wu, W.N. Lennard, D. Landheer, M.W.C. Dharma-Wardana, *J. Appl. Phys.* **107**, 123510 (2010). ☐